

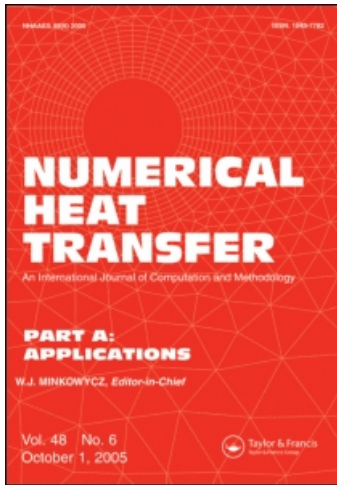
This article was downloaded by: [2007-2008 Korea University - Seoul Campus]

On: 19 November 2008

Access details: Access Details: [subscription number 768980396]

Publisher Taylor & Francis

Informa Ltd Registered in England and Wales Registered Number: 1072954 Registered office: Mortimer House, 37-41 Mortimer Street, London W1T 3JH, UK



Numerical Heat Transfer, Part A: Applications

Publication details, including instructions for authors and subscription information:

<http://www.informaworld.com/smpp/title-content=t713657973>

Numerical Investigation on the Effects of Inlet Air Temperature on Spray Combustion in a Wall Jet Can Combustor Using the k - Turbulence Model

Sangpil Jo ^a; Ho Young Kim ^a; Sam S. Yoon ^a

^a Department of Mechanical Engineering, Korea University, Seoul, Korea

Online Publication Date: 01 January 2008

To cite this Article Jo, Sangpil, Kim, Ho Young and Yoon, Sam S.(2008)'Numerical Investigation on the Effects of Inlet Air Temperature on Spray Combustion in a Wall Jet Can Combustor Using the k - Turbulence Model',Numerical Heat Transfer, Part A: Applications,54:12,1101 — 1120

To link to this Article: DOI: 10.1080/10407780802552179

URL: <http://dx.doi.org/10.1080/10407780802552179>

PLEASE SCROLL DOWN FOR ARTICLE

Full terms and conditions of use: <http://www.informaworld.com/terms-and-conditions-of-access.pdf>

This article may be used for research, teaching and private study purposes. Any substantial or systematic reproduction, re-distribution, re-selling, loan or sub-licensing, systematic supply or distribution in any form to anyone is expressly forbidden.

The publisher does not give any warranty express or implied or make any representation that the contents will be complete or accurate or up to date. The accuracy of any instructions, formulae and drug doses should be independently verified with primary sources. The publisher shall not be liable for any loss, actions, claims, proceedings, demand or costs or damages whatsoever or howsoever caused arising directly or indirectly in connection with or arising out of the use of this material.

NUMERICAL INVESTIGATION ON THE EFFECTS OF INLET AIR TEMPERATURE ON SPRAY COMBUSTION IN A WALL JET CAN COMBUSTOR USING THE $k - \epsilon$ TURBULENCE MODEL

Sangpil Jo, Ho Young Kim, and Sam S. Yoon

Department of Mechanical Engineering, Korea University, Seoul, Korea

A three-dimensional numerical study was performed to assess the effects of inlet temperature and equivalence ratio on the spray combustion and subsequent NO_x emission in a wall jet can combustor (WJCC) installed with twin-fluid air-assisted fuel atomizers. The RNG $k - \epsilon$ turbulence model, eddy breakup (EBU) combustion model, and the Zeldovich model of NO_x formation were utilized in the numerical study. The WJCC was implemented with a swirling air jet at the fuel nozzle exit and two other air jets, known as primary and dilute jets, at downstream locations. The inlet air temperature and overall equivalence ratio were varied from 373 to 1000 K and from 0.3 to 0.6, respectively. Our computational study showed that the inlet air of high temperature induced flow acceleration and sufficient jet penetration, which were desirable for achieving uniform temperature distribution at the combustor outlet but unfavorably yielded increased NO_x emission. While the inlet air temperature had no prominent influence on the evaporation rate of the fuel drops in the upstream primary zone, its influence appeared to be prominent further downstream.

1. INTRODUCTION

Spray combustion is widely used in gas turbine combustors, industrial boilers, rocket engines, and internal combustion engines [1–6]. Particularly in a gas turbine application, fuel-air mixing process plays an important role in the overall combustion performance. For example, both the thermodynamic and physical properties of air and fuel, such as pressure, temperature, Reynolds and Weber numbers, injection velocities, air-fuel ratio, and the strength of the swirl number (if the fuel nozzle is the twin-fluid air-assisted type), become the parameters that influence the performance of a combustor. Further, the size distribution of the injected fuel droplets can also influence the characterization of combustion performance.

To address the issues related to the aforementioned influential parameters, empirical data have been generally applied to analyses to obtain better designs of the gas turbine engine. Acquiring the empirical data from experiment is a painstaking job, whose workload is sometimes considered economically low efficient.

Received 12 September 2007; accepted 11 September 2008.

This research was supported by the Combustion Engineering Research Center (CERC) in KAIST. Address correspondence to Ho Young Kim, Department of Mechanical Engineering, Korea University, Anamdong, 5-Ga, Sungbukgu, Seoul, 136–701, Korea. E-mail: kimhy@korea.ac.kr

Further, the applicability of the empirical data is sometimes narrowly confined due to their lack of generality, so that they cannot be readily extended for other unique cases. Experimentally, the difficulty associated with the optical access to the region near billions of droplets mixed with the complex air flow has led engineers to find an alternative way to analyze and evaluate the combustion characteristics and the overall performance of the engine. For these reasons, computational fluid dynamics, relatively at a low cost, is commonly used to obtain consistent and economically viable analyses. In this perspective, a RANS-based model is more practical than either the DNS or the LES model (which requires more computational time of several orders of magnitude), despite the shortcoming of the RANS model in resolving every detailed physics of turbulence. The RANS-based Eulerian-Lagrangian (EL) spray model has long been used and is still popular for two-phase spray modeling. For example, the well known spray code like KIVA [7] is implemented with the RANS-based EL spray model. While this spray code has been commonly applied for analyzing the flow characteristics of an IC-engine [8], it can also be extended for a similar analysis of a gas turbine engine for aerospace application, which is the particular interest of this article. To make an advance in the spray combustion modeling, many research applications are implemented in spray modeling [9, 10] and chemistry [11].

This article is concerned with the numerical modeling for a wall jet can combustor (WJCC) type gas turbine engine [12, 13]. The complexity of the overall flow in the WJCC is increased by the twin-fluid air-assisted nozzle, in which atomization of the liquid fuel is immediately followed by the aerodynamic shear of swirling air. Here, fuel is injected from the inner nozzle without swirling, but swirling air is injected from an annulus, assisting the atomization process of the fuel. Because swirl is a mechanism which enhances turbulent mixing and convective heat transfer, it has been commonly implemented in atomization devices. Further, swirl introduces a stable recirculation region that yields a mechanism for flameholding. The terminology WJCC is derived from the fact that the primary and secondary (or dilution) air jets are injected from the combustor's wall into the centerline of the combustor, where the fuel droplets are premixed with air for efficient combustion; (see Figure 1).

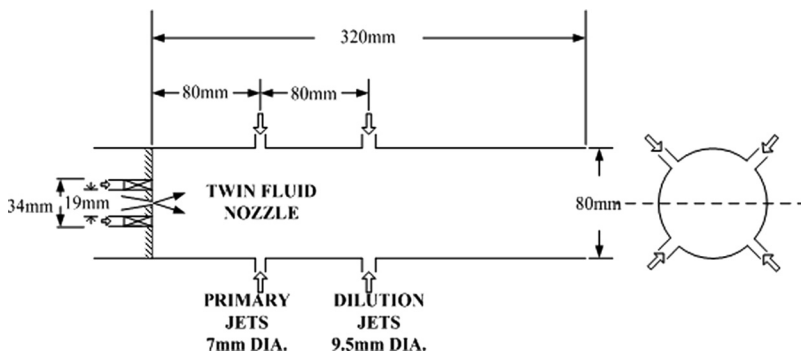


Figure 1. Configuration of the wall jet can combustor (WJCC).

McGuirk and Palma [14, 15] assessed the ability of the $k - \epsilon$ turbulence model to analyze the flow inside gas turbine combustors. They compared their experimental data with their numerical results and found that the maximum error arose in the primary zone, which covered the region from the fuel nozzle exit up to the primary air jet entrance. However, they concluded that the model gave qualitatively acceptable results in other zones of the combustor.

Datta and Som [16] also used the $k - \epsilon$ turbulence model to examine the effect of spray cone angle and drop diameter on wall and exit temperature distributions and combustion efficiency in the combustor. The eddy break-up (EBU) combustion model was used to analyze the burning of n-hexane (C_6H_{14}) fuel in their study. In their following work, Sharma et al. [17] investigated the effect of swirl strength on spray penetration in a WJCC combustor. Spray penetration is often compared for validation of code because of its unique representation of the overall spray characteristics, such as the breakup of ligaments, subsequent evaporation of the droplets, air entrainment, turbulence effect, and finally, fuel-air mixing. The stronger the swirl, the shorter the spray penetration induced because of the relatively stronger recirculatory flow in the upstream side of the combustor. Sharma et al. [17] also reported the effect of gas pressure. The result showed that the spray penetration was shorter with increasing gas pressure because of the greater drag on the traveling droplets and their faster evaporation rate. The data of Cameron et al. [12] and Chang and Chen [18] were used for Sharma et al.'s verification procedure.

To protect the environment, engineers are faced with the major challenge of leveraging NO_x emission to an acceptable level. Datta and Som [19] used the $k - \epsilon$ turbulence model incorporated with the Zeldovich NO_x model [8, 20, 21] to examine the effect of swirl and gas pressure on NO_x emission resulting from the burning of n-hexane within the WJCC combustor. They showed that the increased swirl reduced the NO_x level at the combustor exit, but that the gas pressure had exactly the opposite effect. Their following work [22] showed that decreasing fuel volatility reduced combustion efficiency but increased NO_x emission in WJCC application.

Our present numerical tool is similar to that of Sharma and Som [22] in that the $k - \epsilon$ turbulence model, EBU combustion model, and Zeldovich NO_x model are utilized. The major focus of the current article is to assess the effects of inlet temperature and equivalence ratio on spray penetration, mixing quality, subsequent burning, temperature distribution, and NO_x emission for a given n-decane ($C_{10}H_{22}$) fuel in a

Table 1. Operating conditions

Air flow rate (kg/h)	163
Fuel flow rate (kg/h)	3.27, 6.54
Swirler diameter (mm)	34
Flow split (%)	
Dome swirl	31
Primary jet	30
Dilution jet	39
Swirl number	0.8
SMD (μm)	40
Spray angle (degree)	50
Overall equivalence ratio	0.3, 0.6

WJCC. The fuel is provided through the twin-fluid air-assisted nozzle with swirling air entering the combustor through an annulus of a 60° angle of swirl vanes. The initial SMD value of 40 μm was taken from refs. [12, 23] with the dispersion coefficient of $q = 3.0$ from the Rosin-Rammler size distribution. The details of the initial conditions are listed in Table 1. These comprehensive parametric studies considering the inlet temperature effect have not been found in any previous researches.

2. THEORETICAL MODEL

The basic equations for continuity, momentum, energy, and other properties to be determined can be expressed in a generalized form, known as the steady-state transport equation, sun below.

$$\begin{aligned} & \frac{\partial}{\partial x}(\rho u \phi) + \frac{1}{r} \frac{\partial}{\partial r}(\rho r v \phi) + \frac{1}{r} \frac{\partial}{\partial \theta}(\rho w \phi) \\ &= \frac{\partial}{\partial x} \left(\Gamma_{\phi} \frac{\partial \phi}{\partial x} \right) + \frac{1}{r} \frac{\partial}{\partial r} \left(r \Gamma_{\phi} \frac{\partial \phi}{\partial r} \right) + \frac{1}{r} \frac{\partial}{\partial \theta} \left(\Gamma_{\phi} \frac{\partial \phi}{\partial \theta} \right) + S_{\phi} + S_{l,\phi} \end{aligned} \tag{1}$$

Here, ϕ is a Eulerian property. S_{ϕ} and $S_{l,\phi}$ represent the source terms for the gas and liquid, respectively. Γ_{ϕ} represents the exchange coefficient. The RNG $k - \epsilon$ model [24] is implemented for turbulence modeling, which is suitable for a complex swirling two-phase flow. The details of these variables and terms are listed in Tables 2 and 3.

The Lagrangian phase of the liquid fuel is governed by Newton’s 2 law of motion, assuming that aerodynamic drag is the only external force exerted on a droplet.

$$\frac{d\vec{u}_{di}}{dt} = \frac{3C_D\mu Re}{4\rho_d d_d^2} (\vec{u}_i - \vec{u}_{di}) \tag{2}$$

$$\frac{dx_{di}}{dt} = \vec{u}_{di} \tag{3}$$

Here, \vec{u}_{di} and x_{di} are the droplet velocity and position vector. \vec{u}_i is the instantaneous gas phase velocity defined as the summation of the mean and fluctuating

Table 2. Definition of exchange coefficient and source term of gas phase

ϕ	Γ_{ϕ}	$S_{\phi}/\Delta V$
1	0	0
u	$\mu + \mu_t$	$-\frac{\partial}{\partial x} \left(\bar{p} + \frac{2}{3} \bar{\rho} k + (\mu + \mu_t) \frac{\partial \bar{u}_x}{\partial x_k} \right) + S_u$
v	$\mu + \mu_t$	$-\frac{\partial}{\partial r} \left(\bar{p} + \frac{2}{3} \bar{\rho} k + (\mu + \mu_t) \frac{\partial \bar{u}_r}{\partial x_k} \right) + S_v$
w	$\mu + \mu_t$	$-\frac{\partial}{\partial \theta} \left(\bar{p} + \frac{2}{3} \bar{\rho} k + (\mu + \mu_t) \frac{\partial \bar{u}_{\theta}}{\partial x_k} \right) + S_w$
k	$\mu + \frac{\mu_t}{\sigma_k}$	$G_k - \bar{\rho} \epsilon$
ϵ	$\mu + \frac{\mu_t}{\sigma_{\epsilon}}$	$C_{e1} G_k \frac{\epsilon}{k} - \frac{\bar{\rho} C_{\mu} \eta^3 (1 - \eta/\eta_0) \epsilon^2}{1 + \beta \eta^3} \frac{\epsilon^2}{k} - C_{e2} \bar{\rho} \frac{\epsilon^2}{k}$
Y_i	$\frac{\lambda}{C_p} + \frac{\mu_t}{\sigma_Y}$	S_i

Table 3. Definition of source terms from interphase exchange

ϕ	$S_{d\phi}/\Delta V$	$S_{n\phi}/\Delta V$
1	0	$\frac{1}{\Delta V} \sum_j [\dot{n}_{d,j} S_{m,j}]$
u	$\frac{1}{\Delta V} \sum_j [\dot{n}_{d,j} m_{d,j} (u_{d,j,t+\Delta t} - u_{d,j,t})]$	$\frac{1}{\Delta V} \sum_j [\dot{n}_{d,j} S_{m,j} u_{d,j}]$
v	$\frac{1}{\Delta V} \sum_j [\dot{n}_{d,j} m_{d,j} (v_{d,j,t+\Delta t} - v_{d,j,t})]$	$\frac{1}{\Delta V} \sum_j [\dot{n}_{d,j} S_{m,j} v_{d,j}]$
w	$\frac{1}{\Delta V} \sum_j [\dot{n}_{d,j} m_{d,j} (w_{d,j,t+\Delta t} - w_{d,j,t})]$	$\frac{1}{\Delta V} \sum_j [\dot{n}_{d,j} S_{m,j} w_{d,j}]$
k	$\langle u_i S_{d,u_i} \rangle - \langle u_i \rangle \langle S_{d,u_i} \rangle$	$\langle u_i S_{m,u_i} \rangle - \langle u_i \rangle \langle S_{m,u_i} \rangle + \frac{1}{2} \langle u_i \rangle \langle u_i \rangle \langle S_m \rangle - \frac{1}{2} \langle u_i u_i S_m \rangle$
ε	$1.1 \frac{\varepsilon}{k} S_{d,k}$	$1.1 \frac{\varepsilon}{k} S_{m,k}$
h	$\frac{1}{\Delta V} \sum_j [\dot{n}_{d,j} \{m_{d,j} C_{P,d} (T_{d,j,t+\Delta t} - T_{d,j,t}) + S_{m,j} Q_L\}]$	$\frac{1}{\Delta V} \sum_j [\dot{n}_{d,j} S_{m,j} C_{P,vap} (T_d - T_{ref})]$
Y_{fu}	0	S_m

components. The Reynolds number is defined as

$$Re = \frac{\rho d_d |\vec{u}_i - \vec{u}_{di}|}{\mu} \tag{4}$$

The drag coefficient C_D is chosen from Yuen and Chen [25].

$$C_D(1 + B) = \begin{cases} 24Re(1 + 0.15Re^{0.687}) & Re \leq 1000 \\ 0.44 & Re > 1000 \end{cases} \tag{5}$$

where the factor $(1 + B)$ accounts for the mass flux varying with evaporation due to mass transfer.

The heat and mass transfer of a single droplet are calculated by the equations below [26].

$$\frac{dm_d}{dt} = -\pi d_d \rho D Nu \ln(1 + B) \tag{6}$$

$$m_d C_{Pd} \frac{dT_d}{dt} = \pi d_d \lambda Nu (T - T_d) + \left(\frac{dm_d}{dt}\right) Q_L \tag{7}$$

where D is the binary diffusivity, C_{Pd} is the specific heat of the droplet, λ is the thermal conductivity, and Q_L is the latent heat of vaporization. The Nusselt number, Nu , is obtained from the following correlation [3].

$$Nu(1 + B) = 2 + \frac{0.555 Re^{1/2} (Pr)^{1/3}}{[1 + 1.232 Re^{-1} (Pr)^{-4/3}]^{1/2}} \tag{8}$$

The Spalding mass transfer number, B , is defined as below.

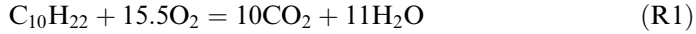
$$B = \frac{(Y_{fu,s} - Y_{fu})}{(1 - Y_{fu})} \tag{9}$$

Assuming steady-state mass and heat transfer to the droplet, diffusion and evaporation are the major phenomena which occur on the droplet surface. The

thermophysical properties of the droplet surface, such as fuel concentration (Y) and so on, can be obtained by assuming that the Clausius-Clapeyron relation [27] describes the change in saturation conditions.

$$Y_{fu,s} = 1/[1 + (P/P_{fu,s} - 1)(W_a/W_{fu})] \quad (10)$$

where P and $P_{fu,s}$ are the operating pressure and the partial pressure of fuel vapor at droplet surface, respectively. Also, W_{fu} and W_a are the molecular weights of the fuel vapor and other species except fuel, respectively. Chemical reaction is assumed to follow the global one-step reaction.



The eddy break-up (EBU) combustion model [28] is adopted, which is incorporated with the RNG turbulence model. The mixing-controlled rate of the reaction is expressed in terms of the turbulence time scale $k - \varepsilon$. The EBU model considers the dissipation rates of fuel, oxygen, and products expressed as given below.

$$\begin{aligned} R_{fu,EBU} &= C_R \bar{\rho} \tilde{Y}_{fu} \frac{\varepsilon}{k} \\ R_{ox,EBU} &= C_R \bar{\rho} \frac{\tilde{Y}_{ox}}{s} \frac{\varepsilon}{k} \\ R_{PR,EBU} &= C'_R \bar{\rho} \frac{\tilde{Y}_{PR}}{1+s} \frac{\varepsilon}{k} \\ C_R &= 4.0, \quad C'_R = 2.0 \end{aligned} \quad (11)$$

where s is the stoichiometric oxygen/fuel ratio by mass basis. Among the various value of R_{EBU} , the slowest is chosen.

$$R_{EBU} = \text{Min}[R_{fu,EBU}, R_{ox,EBU}, R_{PR,EBU}] \quad (12)$$

While the EBU model considers turbulent mixing, the Arrhenius model accommodates kinetically controlled reactions. The Arrhenius reaction rate of n-decane is expressed as below.

$$R_{ARR} = 3.8 \times 10^{14} W_{fu} C_{fu}^{0.25} C_{ox}^{1.5} \exp\left(-\frac{1.2553 \times 10^8}{RT}\right) \quad (13)$$

where C is the molar concentration.

The reaction rate is taken to be the minimum of the EBU and Arrhenius reaction rates.

$$R_{fu} = \text{Min}[R_{EBU}, R_{ARR}] \quad (14)$$

The Zeldovich model [8] for NO_x formation is used because of its simplicity and the wide range of applicability. The Zeldovich mechanism is shown below.



With the quasi-steady assumption for [N] atom, the overall rate for thermal *NO* reaction is

$$\frac{d[NO]_T}{dt} = 2K_1[O][N_2] \left(1 - \frac{K_{-1}K_{-2}[NO]^2}{K_1K_2[O_2][N_2]} \right) / \left(1 + \frac{K_{-1}[NO]}{K_2[O_2] + K_3[OH]} \right) \quad (15)$$

[OH] and [O] radicals are determined with partial equilibrium assumption of ref. [29] as given below.

$$[OH] = 2.129 \times 10^2 T^{-0.57} \exp(-4595/T) [O]^{0.5} [H_2O]^{0.5} \quad (16)$$

$$[O] = 3.97 \times 10^2 T^{1/2} [O_2]^{1/2} \exp(-31090/T) \quad (17)$$

One of the important aspects of gas temperature distribution is its influence over the reliability of turbine inlet guide vanes. If the temperature distribution is not as uniform, but rather stiff, then it would have an adverse effect on the reliability of the turbine blades, which encounter extremely hot gases flowing from the upstream combustor. This scenario would impose a gradual and fatal deterioration of the turbine blades. To prevent this thermal damage, air jets are generally installed to mix and dilute fuel with air in a gas turbine combustor. This air jet installation establishes a uniform temperature profile, which mitigates thermal damage on the turbine blades downstream.

To describe the temperature uniformity of the combustor exit, the pattern factor (PF), is introduced.

$$PF = \frac{T_{\text{exit,max}} - T_{\text{exit,mean}}}{T_{\text{exit,mean}} - T_{\text{in}}} \quad (18)$$

where $T_{\text{exit,max}}$ is the maximum temperature at the combustor exit. $T_{\text{exit,mean}}$ is the average temperature at the combustor exit. T_{in} is the average temperature at the combustor inlet. Here, the PF indicates the uniformity of the temperature distribution at the combustor exit. If PF is large, the maximum temperature deviates greatly from the mean value and, thus, the temperature distribution is less uniform. Likewise, if PF is small, the temperature distribution is more likely to be uniform.

3. NUMERICAL DETAILS

The numerical modeling for the two-phase flow was carried out by the Eulerian-Lagrangian method. Figure 2 shows the computational domain used, a sector, in this study. Based on the physical configuration shown in Figure 1, four air jets are located 90° apart in the circumferential direction, and, therefore, the symmetric flow behavior is presumed in a 90° sector of Figure 2. The primary and dilution air jets were injected at $x = 80$ and 160 mm, respectively, as shown in Figure 1. The axial length extends to 11 radii of the cylindrical sector, allowing sufficient physical space to prevent unnecessary disturbance being bounced back to the upstream domain. As

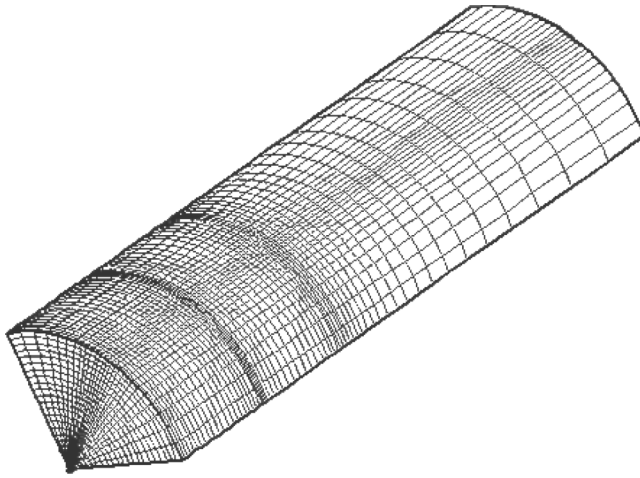


Figure 2. Grid system used for modeling WJCC.

for ignition, n-decane fuel is auto-ignited due to hot surrounding gas of 700 K; auto-ignition temperature of n-decane is about 483 K [30]. The grid resolution of $65 \times 24 \times 27$ (supplying 42,120 nodes in total) is used in the axial, radial, and circumferential directions, which is optimized based on the grid sensitivity study shown in Figure 3. The grid is stretched toward air jets injection locations to better enhance the resolution near the inlets (e.g., twin-fluid nozzle exit, primary, and dilution air jets). Grid smoothing is applied to minimize the numerical error caused by the distortion in orthogonality in the transformed coordinate spaces.

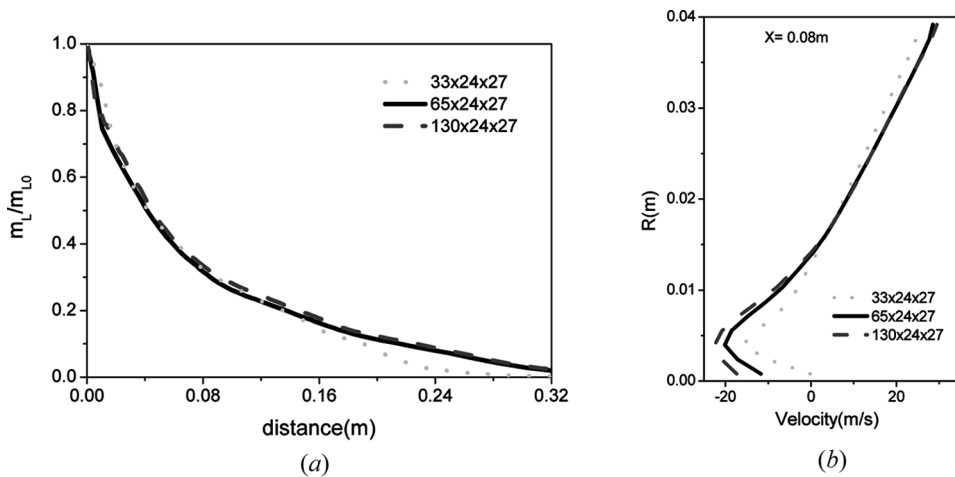


Figure 3. Grid sensitivity test. (a) Normalized liquid fuel flow rate and (b) axial velocity at primary hole $x = 0.08$.

4. RESULTS AND DISCUSSIONS

4.1 Validation for Evaporating Spray in Heated Turbulent Air

The experimental SMD data of Sommerfeld and Qiu [31] for an evaporating and nonreacting isopropyl-alcohol spray in a turbulent air stream of hot temperature were also used for the validation of the current spray model. The type of the spray nozzle was a hollow-cone atomizer. Among the data of several test cases in Table 1 of ref. [13], the data of case 2 were chosen for modeling validation. The operating conditions included 28.3 g/s (7.86 kg/hr) and 0.44 g/s (0.12 kg/hr) air and liquid mass flowrates, respectively, 18 m/s max air velocity, and 100°C and 34°C max air and liquid temperatures, respectively.

The radial profile of SMD and mass flowrate change of the liquid due to droplet evaporation are compared in Figures 4 and 5, respectively. The early upstream SMD profile shows two peaks, whose pattern is typical of a hollow cone spray, but the strong inward motion of the annular air jet hinders the radial spread of the spray.

As shown in Figure 4, there is a clear segregation of the smaller particles in the inner region of the spray, but the larger particles are able to move to the outer regions of the spray. With increasing downstream distance measured (from $x = 25$ to 300 mm), the distribution of the droplets becomes substantially more uniform. Large particles are dispersed by the spray initial cone angle and subsequent interactions with turbulent eddies in the entrained air, while smaller particles are generally swept toward the spray centerline by aerodynamic drag interactions with the entrained air. In addition, the evaporation of small droplets and their subsequent removal caused a more uniform SMD distribution in the radial direction. The experimental data show excellent agreement with the model results up to $x = 100$ mm, but the model results deviate from the experimental data with discernable margin for $x > 100$ mm. This discrepancy was probably due to the model's inability to capture the entrainment details near the center, whose physics would have evaporated the smaller droplets and yielded a more uniform SMD distribution as in the experimental data.

In Figure 5, the change in liquid mass flow rate, normalized by its initial value, as a function of x is plotted, and the model result and the experimental data

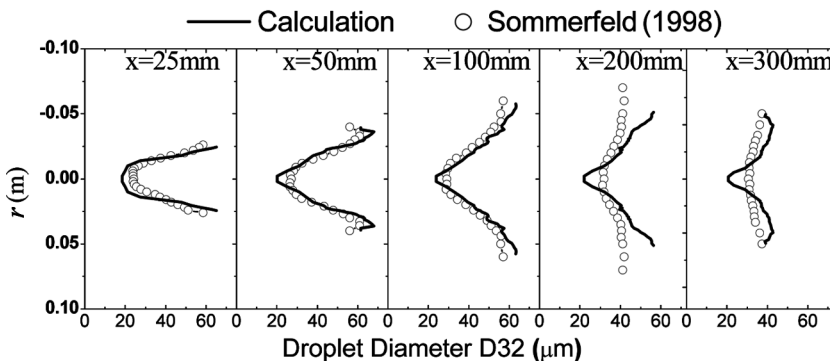


Figure 4. Sauter mean diameter radial profile varying with axial distance.

Downloaded By: [2007-2008 Korea University - Seoul Campus] At: 02:44 19 November 2008

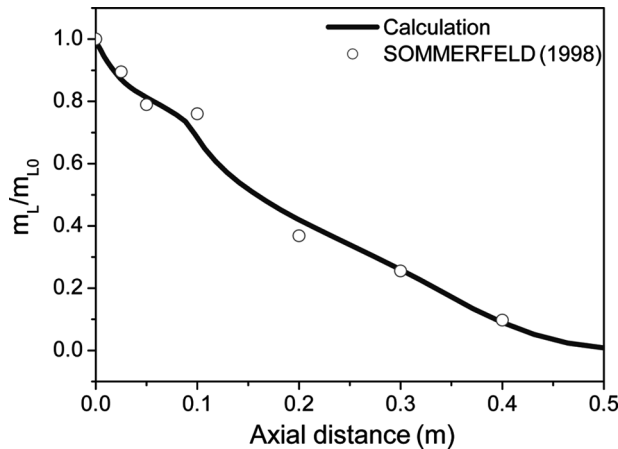


Figure 5. Mass flow rate of spray varying with axial distance.

are compared. The accuracy of the model lies within 2% error. Interestingly, the mass flowrate was accurately predicted at $x = 200$ and 300 mm despite some margin of discrepancy shown in the SMD comparison. This fact indicates that the model predicted the overall evaporation rate accurately even if particle dispersion and dynamics may not have been as accurate.

4.2. Validation for WJCC

In the previous section, spray dynamics and evaporation rate were validated against the experimental data of Sommerfeld and Qiu [31]. Having fair confidence in our model's ability in correctly predicting particle dynamics and evaporation rate, we proceeded to the validation of the "reacting" case in ref. [13] for real WJCC spray combustion.

Both the computed and experimental data of the mean axial velocity as a function of the axial direction, $u_x = u_x(x)$, at the centerline are shown in Figure 6; the margin of deviation lies within 10% error. Most velocities are negative up to the primary air jet injection location ($x = 0.08$ m) due to the adverse pressure gradient. After approximately $x \approx 0.09$ m, the velocity became positive by retaining its stream-wise momentum, but another sudden "dip" is followed in the region near where the dilution air jet is injected.

Figure 7 also shows the mean axial velocity profiles as a function of radial location, $u_x = u_x(r)$, at various axial locations (i.e., $x = 0.05$, 0.08 , 0.12 , and 0.2 m) in relation to Figure 6. Note that the region from the centerline up to the bottom of the shaded box (which is called "split") is the fuel passage of the nozzle, and the upper X-marked box represents the air-assisted swirl annulus. Adverse pressure gradient is clearly shown for the $x = 0.05$ and 0.08 m cases. In the primary zone (i.e., $0 < x < 0.08$ m, from the nozzle exit to the primary air jet injection location), flow accelerates near the wall, except in the recirculation zone, due to enhanced swirling motion. The comparison seems to be qualitatively satisfactory, especially in the

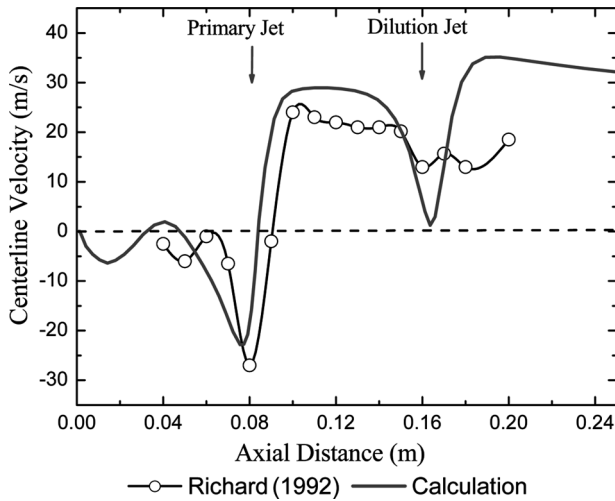


Figure 6. Centerline velocity varying with axial distance.

primary zone. The discrepancy shown at $x=0.05$ m upstream probably originated from the exclusion of the effect of the split positioned between the nozzle fuel passage and the swirling air annulus, resulted from low grid resolution. The error shown at farthest downstream $x \sim 0.2$ m is due to the model's inability to capture the entrainment details because of the low grid resolution.

4.3. Effect of Air Jets Temperature

The computed mean axial velocities at $x = 0.05, 0.08, 0.12,$ and 0.20 m for various air jets temperatures is shown in Figure 8. Here, the air jets include the swirling

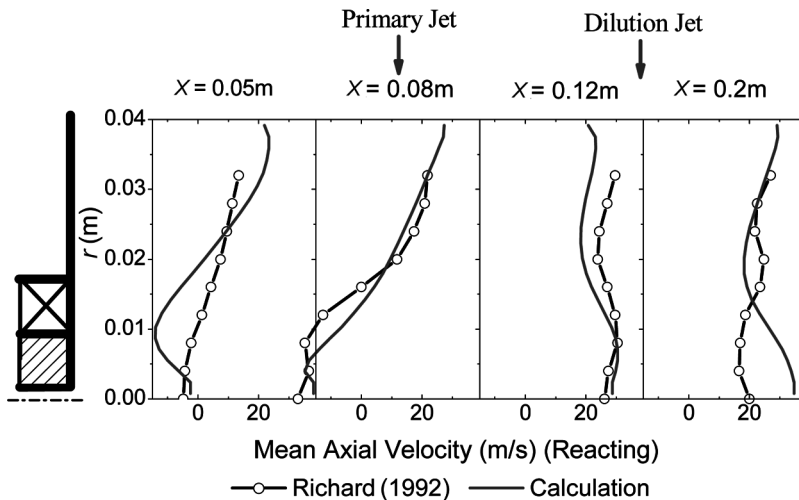


Figure 7. Radial profile of mean axial velocity at various axial locations.

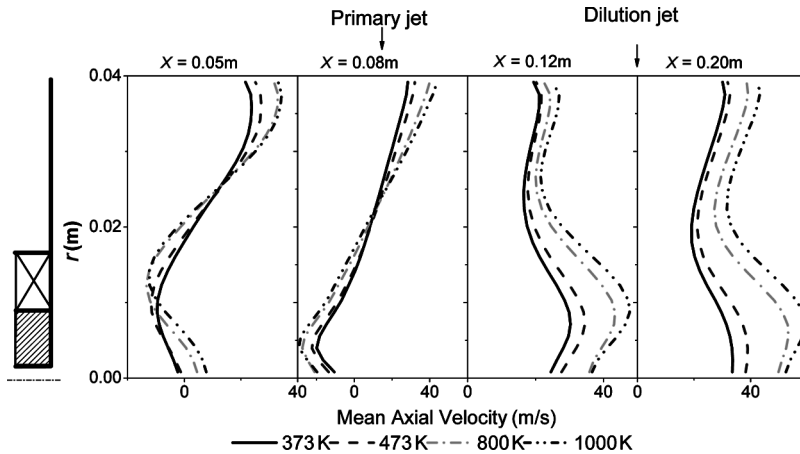


Figure 8. Effect of inlet air temperature on mean axial velocity profiles in both axial and radial directions.

air-assisted jet from the nozzle, primary jet, and dilution jet. These air jet temperatures are varied from 373, 473, 800 K–1000 K. The near wall velocity is high in the upstream (e.g., $x < 0.08$ m) because of the enhanced swirling effect, as mentioned earlier. At $x = 0.12$ m, the centerline velocity gained momentum from the injection of the primary and dilution jets.

When air jet temperature increases, one may expect that the air density would decrease under the fixed 1 atm pressure of the WJCC (e.g., $P = \rho RT$), and thus, yield less drag on the traveling droplets (e.g., $F_D \propto \rho$), resulting in faster droplets. In addition, the air density decrease would also increase the air's inlet velocity because of mass conservation (e.g., $\dot{m} = \rho VA$). This expected flow behavior with changing air temperature is shown in Figure 8; the flow velocity is greater in magnitude (whether it is positive or negative) with greater temperature of air.

The velocity vectors are shown in Figures 9 and 10 for 1000 and 373 K inlet temperatures of air, respectively. For 1000 K, high velocity and deep jet penetration are observed with intense vortices or recirculations residing at various axial locations, including the very upstream at the dome corner like the vortices of a classical step flow. On the other hand, for 373 K, vortices are readily formed, except at the center region of collision between the primary jet and the main stream.

It is noteworthy that vortices are formed in the primary zone when the primary jet collides with the main stream. The presence of these vortices is essential for stable

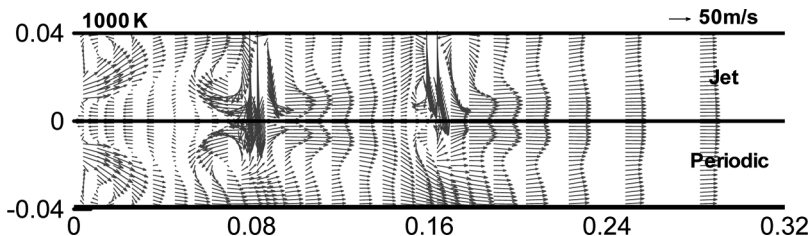


Figure 9. Velocity vector with given inlet air temperature of 1000 K inside WJCC.

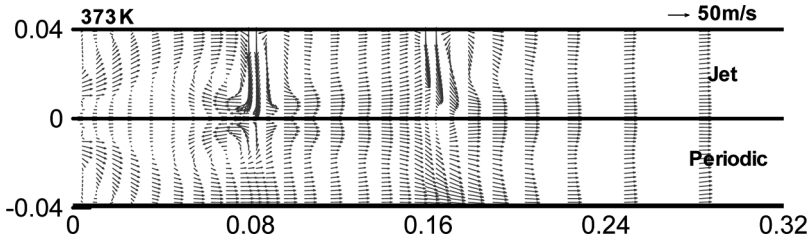


Figure 10. Velocity vector with given inlet air temperature of 373 K inside WJCC.

combustion. The primary zone is known as the primary-jet-driven or the swirl-flow-driven zone, depending on the strength of the vortices. For example, if strong vortices arise, shown in Figure 9 (1000 K), then the primary zone is a primary-jet-driven zone. On the other hand, if weak vortices arise as shown in Figure 10 (373 K), then the primary zone is a swirl-flow-driven zone.

Figure 11 shows the mean temperature profile as a function of the radial location, $T=T(r)$, at various axial locations under fixed $\phi = 0.3$. Temperature increases nearer to the wall, except at $x=0.015$ m. Near the upstream location as in $x=0.015$ m, the temperature fluctuates due to the vortical motion of the flow mixed with freshly injected relatively cold fuel. Further, because this temperature fluctuation magnifies with decreasing inlet air jet temperature, swirl becomes the dominant mechanism that influences this vortical structure at $x=0.015$ m.

Figures 12 and 13 show the isotherms of the two cases mentioned in Figure 11. Dilution zone began downstream from dilution hole. Fresh dilution air was injected into the combustor through the dilution hole. The high temperature gas is diluted in this zone. Therefore, the temperature distribution became more uniform as the hot gas reached the exit of the combustor. In the case of 1000 K, the exit temperature distribution was more uniform.

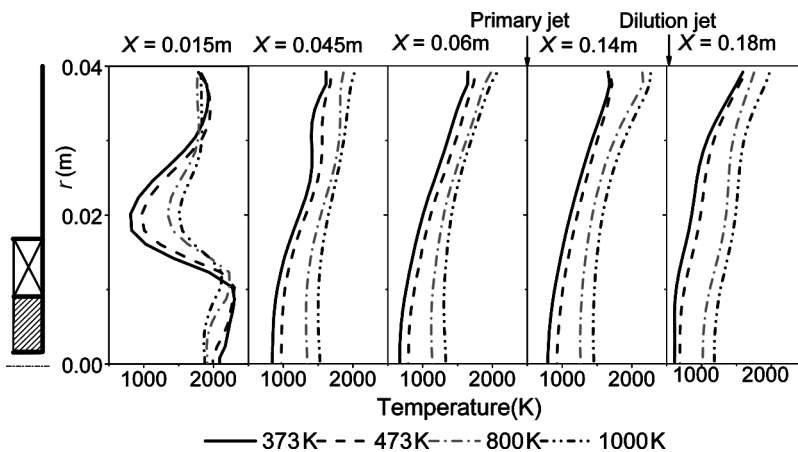


Figure 11. Effect of inlet air temperature on temperature distribution inside WJCC.

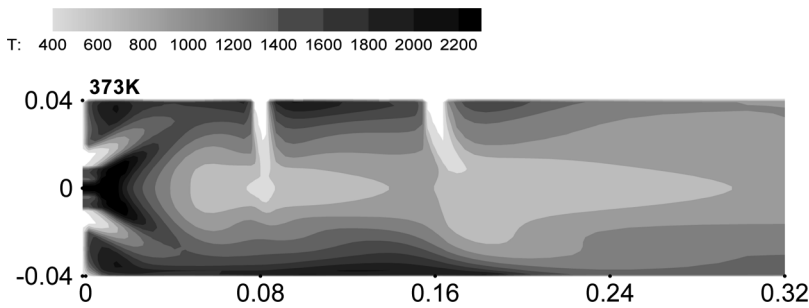


Figure 12. Temperature distribution with given 373 K inlet air temperature and equivalence ratio of $\phi = 0.3$ at periodic plane.

Figure 14 shows the effect of inlet air jet temperature on NO concentration as a function of the axial location. The NO concentration at every axial location was taken as the average of the radial values. With increasing air temperature, the NO concentration was reduced until the point of the primary jet injection, $x = 0.08$ m was reached. While comparing Figures 12 and 13, it is noticed that the high temperature (>1800 K) region at the very upstream of the combustor is relatively larger when the air's inlet temperature is lower; this high temperature produces greater thermal NO_x in the upstream region. However for $x > 0.08$ m, the trend was exactly the opposite. Because the thermal NO_x emissions tended to increase with the rise of the flame temperature, the hottest air near the wall (as in Figures 12 and 13) tended to produce increased amount of NO_x emissions. It seemed that the fuel-air mixing process, intensified by the primary air jet, resulted in the increase of the maximum flame temperature. This situation unfavorably increased the pattern factor, which resulted in less uniformity in the exit temperature distribution and increased NO_x concentration.

4.4. Effect of Equivalence Ratio (or Liquid Fuel Mass Flow Rate)

Figure 15 compares the spray liquid fuel mass flow rate. The solid and dashed lines represent the results obtained by use of the overall equivalence ratios 0.3 and

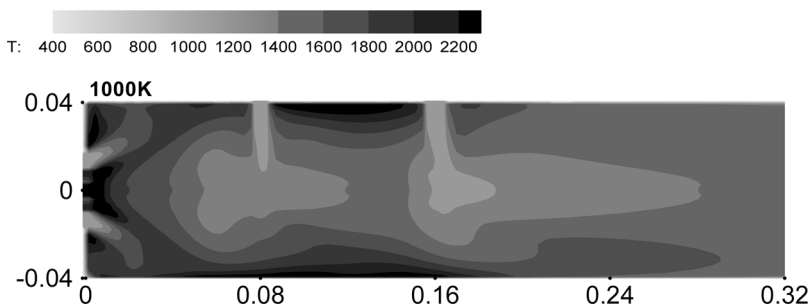


Figure 13. Temperature distribution with given 1000 K inlet air temperature and equivalence ratio of $\phi = 0.3$ at periodic plane.

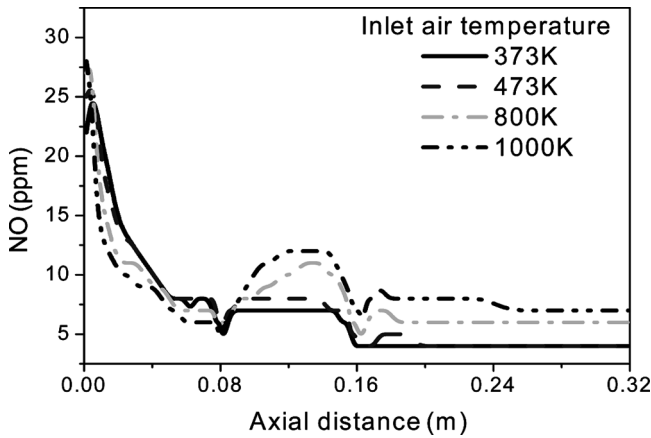


Figure 14. Mean NO concentration varying with axial distance under given $\phi = 0.3$.

0.6, respectively. The mass flow rate was obtained by integrating over the cross sectional area and was normalized by the initial mass flow rate of the spray.

In the primary zone, the difference was not discernable, regardless of variation in the inlet air temperature and the equivalence ratio. However, upon entrance to the secondary zone, prominent difference appeared depending on the inlet air temperature. This trend indicated that the swirling air jet from the annulus had virtually no effect on droplet evaporation; despite the large temperature difference (i.e., 373 K and 1000 K), the mass loss of the droplets to surrounding through evaporation was not significant in the primary zone. However, in the secondary zone (this is the zone located between the primary and dilution jet injection points), the temperature effect was significant and, thus, the droplets exposed to higher air temperature (i.e, 1000 K) evaporated faster. It seemed that the higher equivalence ratio ($\phi = 0.6$) had a slightly greater effect on droplet evaporation for both 373 and 1000 K cases.

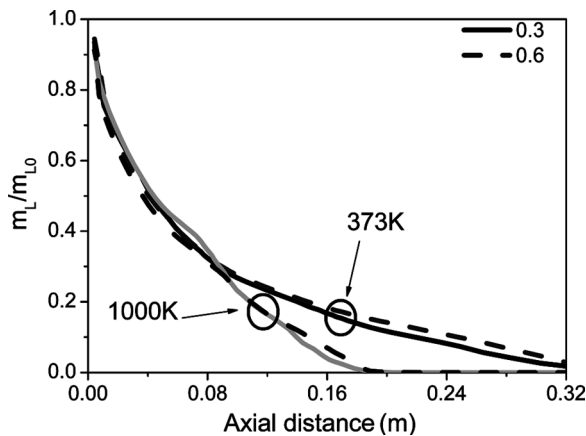


Figure 15. Mass flow rate of the spray varying with axial distance.

The overall effect of equivalence ratio on the droplet evaporation was not significant, even though the low equivalence ratio ($\phi = 0.3$) case yielded slightly quicker droplet evaporation due to relatively excessive air supply (e.g., lean burn). At a high equivalence ratio ($\phi = 0.6$), the relatively excessive fuel supply (but still not a rich burn because $\phi < 1$) slowed the evaporation process of the fuel droplets.

The effects of the inlet air temperature on the pattern factor at two different overall equivalence ratios (i.e., $\phi = 0.3$ and 0.6) are shown in Figure 16. For both $\phi = 0.3$ and 0.6 cases, the pattern factor decreases as the inlet air temperature increases. Thus, increasing the inlet temperature had a favorable effect in producing a more uniform temperature distribution at the combustor exit. Interestingly, the pattern factor is smaller for $\phi = 0.6$ if the inlet air temperature (T_{in}) is less than ~ 675 K. However, the trend is reversed if $T_{in} > 675$ K. Interestingly, more uniform exit temperature (or smaller PF) is yielded for $\phi = 0.6$ than for $\phi = 0.3$ when the inlet air temperature (T_{in}) is less than ~ 675 K, as indicated in Figure 16; we note that this trend at low T_{in} is difficult to observe by comparing Figures 12 and 17. However, the trend is reversed if $T_{in} > 675$ K; the case of smaller $\phi = 0.3$ yielded more uniform temperature distribution. This reversed trend is readily seen by comparing Figures 13 and 18. At 1000 K, the inlet air from the dilution jet takes longer time or distance to mix with the flame when the equivalence ratio is higher because of high temperature gradient, resulted from the extremely high flame temperature; see Figure 18. This is the case at which the mixing process is rather driven by the equivalence ratio than the inlet air temperature. Conversely, at low inlet air temperature (373 K), it takes shorter distance for mixing the inlet air and the flame when the equivalence ratio is higher.

The purpose of the dilution jet is to mix combusted hot gas more uniformly. At a high equivalence ratio (or fuel rich or less oxygen), a relatively larger amount of fuel still would remain unburned and be carried down to the dilution zone at downstream and, then be finally burned. When this occurs, there is no mechanism to dilute the gas of extremely high temperature at this farthest downstream location

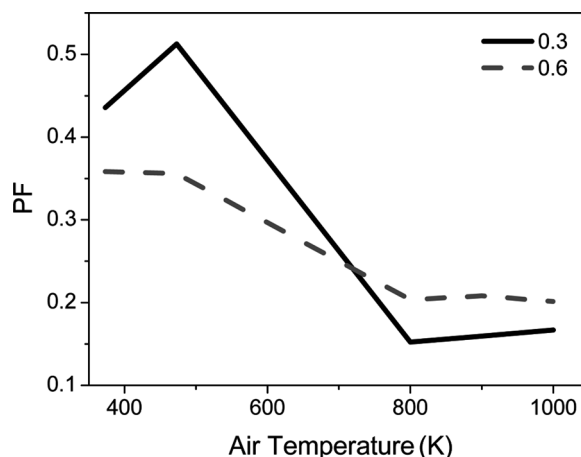


Figure 16. Relation between inlet air temperature with the pattern factor.

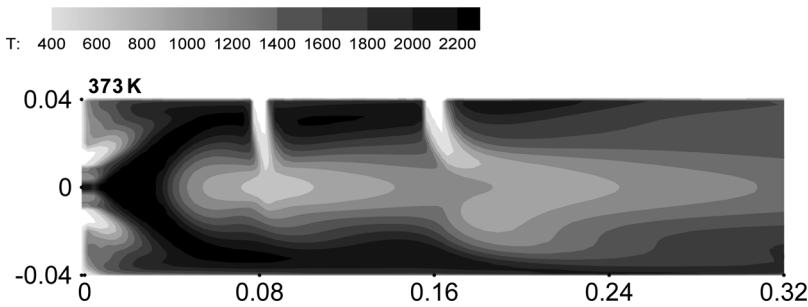


Figure 17. Temperature distribution with given 373 K inlet air temperature and equivalence ration of $\phi = 0.6$ at periodic plane.

and, thus, the pattern factor increases, resulting in a less uniform temperature distribution. In this scenario of high equivalence ratio, a larger amount of NO_x is produced, whose pattern is shown in Figure 19; note, EINO stands for emission index of NO . Also, notice the trend at which the NO_x level increases with increasing inlet air temperature. It should be noted that thermal NO_x emission increases with increasing the flame temperature. Naturally, the greater the fuel supply (high ϕ) is, the greater the flame size, temperature, and, thereby, NO_x emission are. Also, notice the rate at which the NO_x level increases with increasing the inlet air temperature. At relatively low inlet temperature, the effect of ϕ dominates; the greater fuel supply yields the greater NO_x emission. However, as increasing the inlet temperature, its high temperature alone produces enough NO_x even at low $\phi = 0.3$ case that its NO_x level is nearly equivalent to that of $\phi = 0.6$ at 1000 K inlet temperature. Thus, it is inferred that the NO_x level depends strongly on both phi and the inlet air temperature. Further, the difference in NO_x between the 0.3 and 0.6 cases were reduced as the inlet temperature increased. Generally, at a high equivalence ratio, more NO_x is produced when the effect of the inlet air temperature is not considered. However, the higher inlet air temperature also causes the combustion to retain more NO_x . Thus, the two driving mechanisms compete with respect to NO_x production. At a relatively low inlet air temperature, NO_x production is dominated by the equivalence ratio. On the other hand, the NO_x production by the inlet air temperature became increasingly large for the $\phi = 0.3$ case, and the NO_x production of

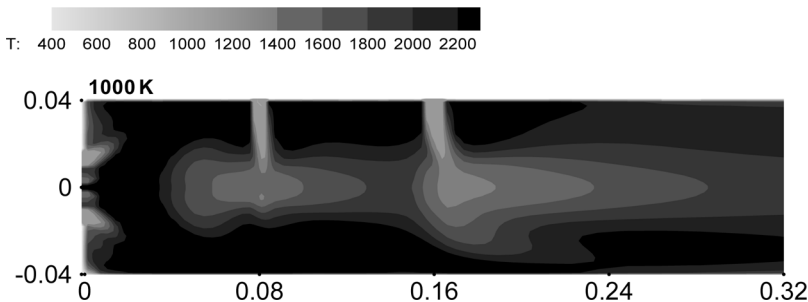


Figure 18. Temperature distribution with given 1000 K inlet air temperature and equivalence ration of $\phi = 0.6$ at periodic plane.

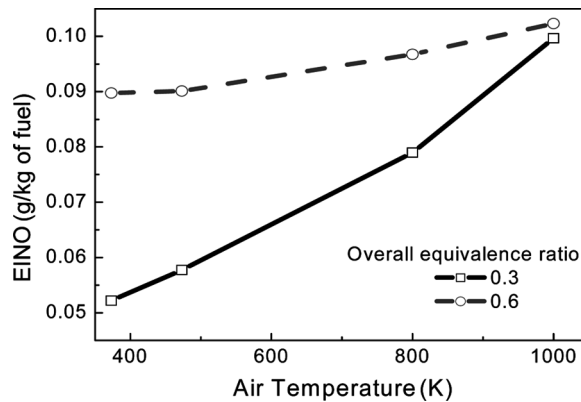


Figure 19. NO emission variation with inlet air temperature.

$\phi = 0.6$ is finally caught up, and eventually NO_x production between these two cases amount to fairly comparable at 1000 K, as in Figure 19.

5. CONCLUSIONS

A three dimensional model for a wall jet can combustor (WJCC) was conducted using a RNG $k - \epsilon$ model for turbulence, eddy breakup model for combustion, and Zeldovich model for NO_x emission. The major focus of this paper was to assess the effects of inlet temperature and equivalence ratio on spray penetration, mixing quality, subsequent burning, temperature distribution, and NO_x emission for given n-decane ($C_{10}H_{22}$) fuel in a WJCC. The computational results are summarized as below.

1. For higher inlet temperatures, high flow velocity and deeper jet penetration were observed, which induced more vortices or recirculation zones in the combustor.
2. As the air temperature increased, the NO_x level reduced in the primary zone, but its level increased predominantly for the rest of the combustor. This behavior of NO_x increase with greater air temperature was more prominent for the low equivalence ratio case.
3. At high equivalence ratios, the NO_x emission was dominated by the equivalence ratio (less oxygen case) rather than by the air temperature.
4. The model also captured the relative dispersion of the larger and smaller particles with good reliability for use in the comparisons of SMD, evaporation rate of the droplet, and flow velocity of both reacting and non-reacting cases.

REFERENCES

1. C. K. Law, Recent Advances in Droplet Vaporization and Combustion, *Prog. Energy Combust. Sci.*, vol. 8, pp. 171–201, 1982.
2. W. A. Sirignano, Fuel Droplet Vaporization and Spray Combustion Theory, *Prog. Energy Combust. Sci.*, vol. 9, pp. 291–322, 1983.

3. G. M. Faeth, Current Status of Droplet and Liquid Combustion, *Prog. Energy Combust. Sci.*, vol. 3, pp. 191–224, 1977.
4. G. M. Faeth, Evaporation and Combustion of Sprays, *Prog. Energy Combust. Sci.*, vol. 9, pp. 1–76, 1983.
5. G. M. Faeth, Mixing, Transport and Combustion in Sprays, *Prog. Energy Combust. Sci.*, vol. 13, pp. 293–345, 1987.
6. H. H. Chiu, Advances and Challenges in Droplet and Spray Combustion, I. Toward a Unified Theory of Droplet Aerothermochemistry, *Prog. Energy Combust. Sci.*, vol. 26, pp. 381–416, 2000.
7. P. J. O'Rourke, Collective Drop Effects on Vaporizing Liquid Sprays, Ph.D. thesis, Princeton University, 1981.
8. R. D. Reitz and C. J. Rutland, Development and Testing of Diesel Engine CFD Models, *Prog. Energy Combust. Sci.*, vol. 21, pp. 173–196, 1995.
9. D. J. Glaze, S. S. Yoon, J. C. Hewson, and P. E. DesJardin, Modeling Transport Phenomena of High Mass Loadings with Applications to Fire Suppression, *Numer. Heat Transfer B*, vol. 53, no. 2, pp. 118–142, 2008.
10. A. K. Tolpadi, S. K. Aggarwal, and H. C. Mongia, An Advanced Spray Model for Application to the Prediction of Gas Turbine Combustor Flow Field, *Numer. Heat Transfer A*, vol. 38, no. 4, pp. 325–340, 2000.
11. M. S. Raju, On the Importance of Chemistry/Turbulence Interactions in Spray Computations, *Numer. Heat Transfer B*, vol. 41, no. 5, pp. 409–432, 2002.
12. C. D. Cameron, J. Brouwer, C. P. Wood, and G. S. Samuelsen, A Detailed Characterization of the Velocity and Thermal Fields in a Model Can Combustor with Wall Jet Injection, *ASME J. Eng. Gas Turbine Power*, vol. 111, pp. 31–35, 1989.
13. C. D. Richards and G. S. Samuelsen, The Role of Primary Jets in the Dome Region Aerodynamics of a Model Can Combustor, *ASME J. Eng. Gas Turbine Power*, vol. 114, pp. 20–26, 1992.
14. J. J. McGuirk and J. M. L. M. Palma, Experimental Investigation of the Flow inside a Water Model of a Gas Turbine Combustor: Part 1 – Mean and Turbulent Flow field, *J. of Fluids Eng.*, vol. 117, pp. 450–458, 1995.
15. J. J. McGuirk and J. M. L. M. Palma, The Flow Inside a Model Gas Turbine Combustor: Calculations, *ASME J. Eng. Gas Turbine Power*, vol. 115, pp. 594–602, 1993.
16. A. Datta and S. K. Som, Effects of Spray Characteristics on Combustion Performance of a Liquid Fuel Spray in a Gas Turbine Combustor, *Int. J. Energy Res.*, vol. 23, pp. 217–228, 1999.
17. N. Y. Sharma, A. Datta, and S. K. Som, Influences of Spray and Operating Parameters on Penetration of Vaporizing Fuel Droplets in a Gas Turbine Combustor, *Appl. Thermal Eng.*, vol. 21, pp. 1755–1768, 2001.
18. K. C. Chang and C. S. Chen, Development of a Hybrid $k - \epsilon$ Turbulence Model for Swirling Recirculating Flows under Moderate to Strong Swirl Intensities, *Int. J. Numer. Meth. Fluids*, vol. 16, pp. 421–443, 1993.
19. A. Datta and S. K. Som, Combustion and Emission Characteristics in a Gas Turbine Combustor at Different Pressure and Swirl Conditions, *Appl. Thermal Eng.*, vol. 19, pp. 949–967, 1999.
20. R. R. Raine, C. R. Stone, and J. Gould, Modeling of Nitric Oxide Formation in Spark Ignition Engines with a Multizone Burned Gas, *Comb. and Flame*, vol. 102, pp. 241–255, 1995.
21. L. J. Muzio and G. C. Quartucy, Implementing NO_x Control: Research and Application, *Prog. Energy Combust. Sci.*, vol. 23, pp. 233–266, 1997.

22. N. Y. Sharma and S. K. Som, Influence of Fuel Volatility and Spray Parameters on Combustion Characteristics and NO_x emission in a Gas Turbine Combustor, *Appl. Thermal Eng.*, vol. 24, pp. 885–903, 2004.
23. C. D. Cameron, J. Brouwer, and G. S. Samuelen, A Model Gas Turbine Combustor with Wall Jets and Optical Access for Turbulent mixing, Fuel Effects, and Spray Studies, Twenty-Second Symposium (International) on Combustion, Seattle, WA, USA, vol. 1, pp. 465–474, The Combustion Institute, Pittsburgh, Pennsylvania, 1988.
24. Z. Han and R. D. Reitz, Turbulence Modeling of Internal Combustion Engines Using RNG $k - \epsilon$ Models, *Comb. Sci. and Tech.*, vol. 106, pp. 267–295, 1995.
25. M. C. Yuen and L. W. Chen, On Drag of Evaporating Liquid Droplets, *Comb. Sci. and Tech.*, vol. 14, pp. 147–154, 1976.
26. A. Berlemont, M. S. Grancher, and G. Gouesbet, On the Lagrangian Simulation of Turbulence on Droplet Evaporation, *Int. J. Heat and Mass Transfer*, vol. 34, pp. 2805–2812, 1991.
27. K. K. Kuo, *Principles of Combustion*, pp. 94, 95, 378, John Wiley & Sons, New York, 1986.
28. B. F. Magnussen and B. H. Hjertager, On Mathematical Modeling of Turbulent Combustion with Special Emphasis on Soot Formation and Combustion, Sixteenth Symposium (International) on Combustion, Cambridge, Massachusetts, pp. 719–729, The Combustion Institute, Pittsburgh, Pennsylvania, 1976.
29. J. B. Heywood, *Internal Combustion Engine Fundamentals*, pp. 572–577, McGraw-Hill, Singapore, 1988.
30. S. K. Aggarwal, A Review of Spray Ignition Phenomena: Present Status and Future Research, *Prog. Energy Combust. Sci.*, vol. 24, pp. 565–600, 1998.
31. M. Sommerfeld and H. H. Qiu, Experimental Studies of Spray Evaporation in Turbulent Flow, *Int. J. Heat and Fluid Flow*, vol. 19, pp. 10–22, 1998.